

# Characterization of Mechanical Properties, Macroscopic Deformation Behavior, and Microstructure of Functionally Graded 22MnB5 Steel

Emad Scharifi,\* Thomas Schade, Agim Ademaj, Seyed Vahid Sajadifar, Ursula Weidig, Thomas Niendorf, and Kurt Steinhoff

The focus of this study is on the characterization of the local plastic deformation and failure of functionally graded 22MnB5 plates after hot stamping using an in situ approach. Various forming strategies at elevated temperatures are performed using differentially tempered forming tools to locally tailor the microstructure. By controlling the cooling rate, graded as well as martensitic and ferritic–pearlitic microstructures are obtained. Experimental analysis includes evaluation of the material- and geometry-dependent local strain evolution by tensile tests coupled with digital image correlation conducted on two different sample geometries, tapered and nontapered. Experimental results reveal a much more complex deformation behavior for the functionally graded than for homogenous samples. As expected, the distribution of plastic strain of the graded sample is depending on the mixture of its constituting microstructures; however, different types of localized failure after necking are found. Obviously, failure evolution also depends on the sample geometry. Failure patterns observed include shear bands, crossed bands, or homogenous localization of strain, i.e., traditional necking. Eventually, in the case of the nontapered geometry, a lower level of local plastic strain with multiple necking sites is observed. Based on findings presented, detailed process-microstructure-property-damage relationships are established.

## 1. Introduction

The ongoing global trend toward carbon dioxide emission reduction forced the automotive industry to design lighter and resource-efficient vehicle bodies, leading to the huge success of the press hardening process.<sup>[1–5]</sup> One reason for this success lies in the availability of thin-walled ultra-high strength steel 22MnB5, which combines good formability and highest strength properties of 1500 MPa at a fully martensitic structure after press hardening at reasonable costs.<sup>[6,7]</sup> Since the first application in the automotive industry in 1986 as a side-impact beam,<sup>[8]</sup> the application field of 22MnB5 components increases continuously from B-pillar to roof rail reinforcement and other parts to enhance passenger safety.<sup>[9,10]</sup>

The thermomechanical approach of press hardening allows the production of complex-shaped components with high dimensional accuracy,<sup>[11]</sup> excellent mechanical properties, and, at the same time, offers the opportunity for realizing tailored properties.<sup>[12,13]</sup> Although a time–temperature


course of uniform austenitization and quenching in a cooled forming tool, **Figure 1a**, results in a homogenous fully martensitic structure with highest strength, a locally varying time–temperature course during the forming process, **Figure 1b**, enables the creation of a tailored distribution of microstructures, where mechanical properties are locally adjusted to perfectly meet the load profile, e.g., in case of crash-relevant components.<sup>[5,6]</sup> According to Ademaj et al., after uniform austenitization at 930 °C but differential cooling of 22MnB5, zones following “route H” develop highest tensile strengths (1500 MPa) whereas zones following “route S” show lower tensile strength properties (614 MPa).<sup>[14]</sup> Both process strategies of **Figure 1** are chosen for the current study with respect to the aforementioned investigations.

This approach has been identified as a viable option to obtain lighter body structures through the ability to design load adapted structures and to combine contradictory requirements within one component.<sup>[14,15]</sup> A prominent example in car body structures is the B-pillar, in which the bottom section exhibits higher

E. Scharifi, T. Schade, Dr. U. Weidig, Prof. K. Steinhoff  
Metal Forming Technology  
University of Kassel  
Kurt-Wolters-Straße 3, Kassel 34125, Germany  
E-mail: emad.scharifi@uni-kassel.de

A. Ademaj  
Metakus Automotive GmbH  
Fehrenberger Straße 1a, Baunatal 34225, Germany

Dr. S. V. Sajadifar, Prof. T. Niendorf  
Institute of Materials Engineering  
University of Kassel  
Mönchebergstraße 3, Kassel 34125, Germany

 The ORCID identification number(s) for the author(s) of this article can be found under <https://doi.org/10.1002/srin.202000633>.

© 2021 The Authors. Steel Research International published by Wiley-VCH GmbH. This is an open access article under the terms of the Creative Commons Attribution License, which permits use, distribution and reproduction in any medium, provided the original work is properly cited.

DOI: 10.1002/srin.202000633

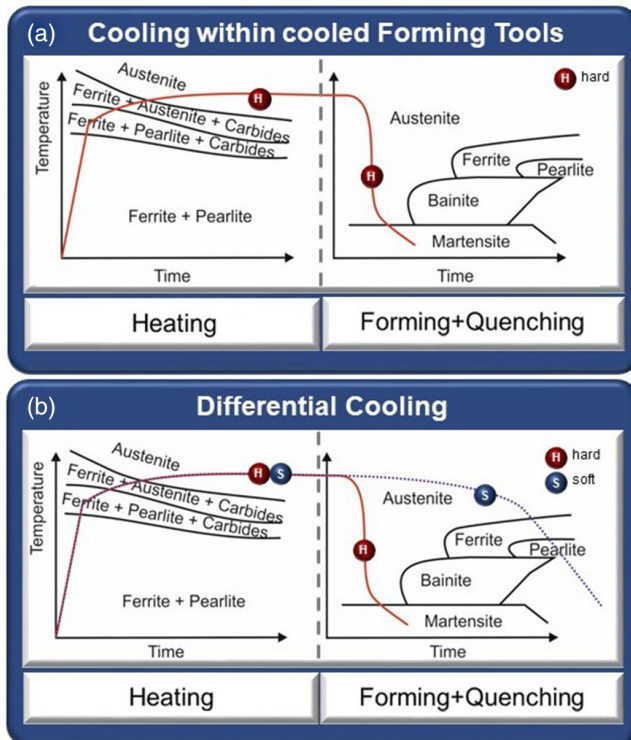


**Figure 1.** a) Schematic illustration of the time–temperature path with cooled forming tools resulting in a fully martensitic microstructure by characteristically high cooling rate, and b) differential cooling to obtain a graded structure by locally differing cooling rates imposed by differentially tempered tools.<sup>[14]</sup> Reproduced with permission.<sup>[17]</sup> © 2014, Verlag Wissenschaftliche Scripten.

energy absorption capacity provided by a soft structure as compared with that of the upper part with hard martensite.<sup>[6,14,16]</sup> This so-called functional gradation directly realized within the press hardening process is an adaptation of the concept, which was first introduced by the National Space Laboratory in Japan in the field of powder and melt metallurgy.<sup>[16,17]</sup> In this context, Steinhoff et al. discerned between a graded material, featuring a property change over at least one macroscopic dimension, and functional gradation where these property changes follow the objective of achieving an application-oriented adjustment of product properties.<sup>[3,18]</sup> In metal forming technology, a viable source for the functional gradation can be traced by the defined thermomechanical processing.<sup>[19]</sup> Hence, the possible combination of differential thermal control during an integrated forming operation at elevated temperatures enables the extremely efficient production of components with tailored properties.<sup>[20]</sup> Since the first application, press hardening of tailored properties is a globally growing trend with an increasing number of scientific and industrial studies reporting on the adjustment of locally varying mechanical properties for press hardened 22MnB5 steel. In these studies, the influence of cooling rates on the mechanical properties has been evaluated in depth.<sup>[4,20–24]</sup> It was shown that the load adapted distribution of strength and ductility in case of the final part can be achieved by different contact cooling conditions during the forming step, e.g., using segmented tempered forming tools, which eventually promote the locally different

phase transformations.<sup>[12,25]</sup> High local cooling rates, well above  $30\text{ }^{\circ}\text{C K}^{-1}$ , lead to the formation of very hard martensitic structures, whereas lower local cooling rates result in more ductile microstructures, i.e., ferrite and pearlite.<sup>[10,26]</sup> This behavior has been already analyzed by use of a numerical model focusing on pathways toward tailored tempering proposed by Tang et al. In their study, the authors evaluated the differential phase transformation of 22MnB5 by variable cooling rates.<sup>[27]</sup>

However, despite the benefits of tailoring mechanical properties of the components, it is obvious that, induced by the increase in the volume fraction of hard phases, a generally low formability on the global scale and concomitantly low strains to necking and failure are the consequences. So far, only a few publications address characterization of the particular mechanical behavior of such functionally graded components focusing on local analysis of properties. For instance, George et al. used quasi-static tensile tests for investigating the differing deformation behavior based on miniature tensile specimen taken from the soft and the hard zone of the component.<sup>[28]</sup> Min et al. and Eller et al. utilized a similar method for their investigations on graded materials.<sup>[28,29]</sup> To obtain force–displacement relations for the validation of their finite element analysis model of graded 22MnB5 material conditions, they coupled their tensile tests with a digital image correlation (DIC) system.<sup>[29,30]</sup> Tapered tensile sample geometries with two different gauge section widths were chosen for the purpose of influencing the location of plastic deformation and to eventually ensure that the necking zone occurred within the gauge length. Comparing experimental results with the simulation of these tensile tests concerning force–displacement curves and fracture location, they stated a good agreement for both geometries. By the exclusive use of tapered samples for functionally graded microstructures, only one single deformation localization was detected in their tests which resulted in the final fracture location. However, multiple necking phenomena as well as change in deformation locations and differing failure patterns were not mentioned.<sup>[20,21]</sup> Thus, the detailed determination of the displacement field, particularly of the transition zone, during plastic deformation of graded structures is limited. Consequently, the complex dissimilar deformation mechanisms of the inhomogeneous microstructure of 22MnB5 occurring during straining in the transition zone remain unlighted.

A large number of scientific studies in this regard were conducted to reveal the morphological and crystallographic changes upon deformation of different high strength steels containing dissimilar phases by the use of in situ deformation experiments and crystal plasticity simulation.<sup>[31–33]</sup> Tasan et al., for example, have shown that microstructural strain distribution of dual-phase (DP) steels strongly depends on the martensite distribution and the ferritic grain sizes during plastic deformation using high-resolution microscopic DIC technique.<sup>[32]</sup> This phenomenon is based on the mixed microstructure containing different phases with different slip systems as well as different phase boundaries.<sup>[34]</sup> For example, the geometric constraints of the martensitic lath structure lead to different slip and deformation processes being active as compared with ferritic body-centered cubic slip systems. Moreover, on the microscopic level, retained austenite, even at a small fraction between martensite and bainite, can influence plasticity within both phases.<sup>[35]</sup> As highlighted earlier,

interface plasticity prevailing in addition to dislocation glide needs to be considered to understand the complex deformation mechanisms of mixed microstructure in depth. Therefore, further scientific studies focused on the deformation behavior of high strength steels by multifield mapping of the final microstructure to provide insights into the microscopic deformation mechanisms and the related damage mechanisms.<sup>[32,34,36]</sup> The authors were able to analyze and characterize the microstrain fields and the associated microstructure by the use of different *in situ* techniques. Among others, such studies included electron backscatter diffraction or electron channeling.

The aforementioned studies are mainly focused on DP and other high strength steels such as martensitic steels; however, similar approaches to study the microstrain and the deformation map of the microstructure of 22MnB5 are missing. To explore the relevant elementary mechanisms, high-resolution microscopes are required to understand the microscopic plastic deformation of 22MnB5 in different phases. Yet, it is clear that these mechanisms significantly influence the macroscopic flow behavior of the material during straining due to morphological changes. Taking the mentioned mechanisms into account, the description of the deformation mechanisms and the nature of plasticity of 22MnB5 on the macroscopic level especially in the transition zones, eventually due to the existence of different phases, are very difficult to characterize. A detailed analysis of the local plastic strain of these steels (22MnB5) on the macroscopic scale provides some details regarding the microstructural changes and failure mechanisms.

In the past, several optical field methods have been developed to evaluate the complex microscopic local flow of a material during plastic deformation and to characterize the necking behavior of metallic materials. Sciammarella et al., for example, proposed two optical techniques to measure the strain by point determination and field methods based on the optical filtering. In both techniques, the final strain distribution imposed by mechanical loading was transferred into light intensity.<sup>[37]</sup>

For the point measurement, a grid pattern was first applied to the surface of the investigated zone. This region was then illuminated by a monochromatic plane wave front, and a convergent lens was placed in the focal length between the principal plane and the measured zone. On the opposite side of the lens, in the focal length, a spectrum of the transmission function of the applied grid pattern was observed, which is the Fourier transform of the grids. This spectrum on the backside consists of a diffraction pattern with an intensity distribution depending on the grid pattern sizes as well as on geometry and the light source. Finally, by changing the grid geometry imposed by external mechanical load and deformation, the spectrum and the maximum intensity of the diffraction are shifted by the amount of the deformation level of the grids and the deformation can be measured.

The field method, on the contrary, requires a printed grid on the sample surface as the carrier of sample displacement, which can be analyzed as a frequency-modulation effect as reported also in other studies.<sup>[37,38]</sup> Here, the strain of the specimen can be determined by the change in the measured intensity. The advantage of this method is that the strains measured using this technique can be determined in three different directions. It was demonstrated that the point-by-point method is suitable for

measuring the strain for displacements, dynamic phenomena as well as at high temperatures.<sup>[39]</sup> In Hung et al.'s study, a coherent optical technique was developed, which enabled the measurement of surface displacement and strain distribution.<sup>[40]</sup> Another technique is the so-called laser speckle photography (LSP), which is based mainly on the high-resolution photographing of speckle patterns to obtain hydrodynamic flow velocity.<sup>[41]</sup> The needed information for determining the movement and the velocity is obtained in this way from the moving pattern inside the medium. During the optical recording of the speckle pattern, a fringe pattern is formed as a result of the flow behavior of the medium, and the distribution of the pattern is related to the velocity field of the medium. This technique has been used for different applications to measure the surficial and geometrical changes.<sup>[41]</sup> Carlson et al. investigated the shear band formation with the help of optical strain measurements in a two-phase material.<sup>[42]</sup> For this purpose, they focused on the lateral changes in the position of a single-phase, i.e., local austenitic fractions, to characterize the overall shape changes on the surface of the sample.

Another promising approach, especially for materials with locally differing properties, is the so-called DIC technique. This method provides for the accurate measurement and mapping of the strain distribution and its changes during elastoplastic deformation. For example, Eisenlohr et al. used DIC in combination with thermal imaging to investigate the local deformation behavior and the corresponding temperature rise of a Fe-3 wt% Si material to establish the correlation between stress drops, temperature evolution, and strain localization during tensile tests.<sup>[43]</sup> In numerous scientific studies, full-field noncontact optical techniques of different kind are applied providing for micrographs to be used for local strain analysis by DIC, to eventually characterize local plasticity, necking, and contour deformation. Thus, during the last decades the DIC technique clearly revealed its huge potential for diverse fundamental studies.<sup>[43-45]</sup>

The DIC technique is characterized by the use of photogrammetry in combination with microstructure analysis during loading. The kinematic changes and the surface feature distribution can be tracked by mapping and recording the prepared sample surfaces by use of a quasi-stochastic pattern.<sup>[46]</sup> Accordingly, the sample surface is then captured by an image processing system applying rectangular grids on the sample surface. Therefore, the facets on the sample surface result in measuring points. During the plastic deformation, geometrical changes are then calculated by a software integrated in the system and the displacement as well as strain distribution are determined.<sup>[46,47]</sup>

The accuracy and precision of this measurement technique depend on several factors, which can be roughly differentiated in factors dependent on the camera system, the measurement setup, the measurement procedure, and environmental perturbations. The overall quality and resolution of the recorded pictures from the investigated zone are important parameters. The accuracy of the DIC in computing the displacement is reported to be in the order of 0.01 pixel.<sup>[48]</sup> An increase in the correlation sub-image strain parameter can further improve the accuracy.<sup>[48]</sup> When only a single camera in front of a specimen is used in 2D DIC measurements, the used angle between the camera and the region of interest as well as the digital image resolution plays an important role. An alignment of the CCD camera at an

angle of 90° to the specimen is recommended to avoid measurement errors as well as a sufficient spatial resolution of the imaging system.<sup>[49]</sup> In case of 2D DIC measurement, an improvement of the accuracy can be achieved by using special algorithms as in detail reported by Khoo et al.<sup>[49]</sup> When it comes to the measurement procedure, the accuracy depends strongly on an appropriate choice of speckle patterns giving a sufficient contrast and resolution as well as it is influenced by suitable straining parameters. Large strain parameters resulting in high strain gradients would lead to measurement errors due to the averaging of local strain field during deformation.<sup>[50]</sup> In addition, thermal noise as well as acoustic vibrations of the surroundings could also influence the CCD camera and, therefore, the accuracy of the measurement.<sup>[51]</sup>

Taking into consideration the details presented earlier, it is obvious that in situ characterization of localized deformation and damage processes enabled by DIC is an appropriate approach to address open questions in the field of the complex deformation behavior of functionally graded high strength steels. The aim of this study is to analyze the local characteristics of plastic strain evolution as well as of damage initiation and damage propagation in ferritic–pearlitic, martensitic, and microstructurally graded 22MnB5 samples. In contrast to the use of tapered samples described by Eller et al.,<sup>[29,30]</sup> also straight samples with constant gauge section dimensions were added for the DIC coupled tensile tests of functionally graded microstructures. To address aspects related to the geometry of real parts, not only straight samples with constant gauge section dimensions but also tapered samples have been considered. Thereby, process–microstructure–property–damage relationships could be established accounting as well for nonhomogenous microstructure distributions, eventually allowing for further improvement of safety and reliability of complex components realized by advanced press hardening processes.

## 2. Experimental Procedure, Testing Methods and Material Description

### 2.1. Material

The experimental investigations in this work were conducted using boron sheet steel 22MnB5 as a representative for the most widely used high strength steel in the automotive industry when it comes to crash-relevant components. The as-received material (ArcelorMittal) is Al–Si coated and characterized by an initial microstructure consisting of homogeneous distribution of ferrite and pearlite, an ultimate tensile strength (UTS) of 610 MPa and elongation after failure of 0.20. The chemical composition, determined by optical emission spectroscopy, is shown in **Table 1**. Upon processing, i.e., press hardening including contact cooling imposed by cooled tools, a fully martensitic structure is obtained

with a UTS of 1600 MPa and elongation after failure of 0.05.<sup>[17]</sup> For the thermomechanical treatments conducted in the current work, the investigated materials were sectioned into blanks of  $500 \times 400 \times 1.5 \text{ mm}^3$ .

### 2.2. Experimental Concept

The experimental setup used in the current work for producing the test samples, **Figure 2**, consists of a roller hearth furnace, a transfer of the heated blanks, and a hydraulic press with a hat-profile tool. The press force was set to 1000 kN and the forming speed to  $48 \text{ mm s}^{-1}$ . The cooling is performed by the tool, which consists of a heated and a cooled section, thermally separated by a small gap. To obtain different microstructures as well as a graded distribution of them, three sets of experimental parameters were selected (**Table 2**).

For reference, the first condition considered was the as-received material with the initial microstructure consisting of ferrite and pearlite. The second set, **Table 2**, targeted a complete homogenous martensitic structure. Consequently, the blanks were austenitized at 870 °C and soaked for 90 s (**Figure 3a**). It should be noted that the furnace temperature was set to 930 °C and the material temperature was measured using thermocouples. After the transfer, within 6–8 s, the blanks were quenched for 10 s in the cooled tool (18 °C). The third set aimed at establishing a graded structure obtained by locally different cooling rates due to the differentially tempered tool (500 and 18 °C, 10 s cooling time) (**Figure 3b**). The fourth set, **Figure 3c**, focused on creating a homogeneous ferritic–pearlitic microstructure after austenitization at 870 °C for 90 s and subsequent cooling in air. The schematic illustration of the all investigated routes and the used parameters is shown in **Figure 3a–c**.

### 2.3. Characterization of Properties and Local Deformation Behavior

Hardness profiles along the longitudinal axes of each sample were obtained from Vickers hardness measurements at a test load of 98.07N (HV10). The profiles were evaluated to highlight the property distribution and to select the section of the hat profile sample for the tensile test (cf., also **Figure 6a**). The area of smallest gauge width was chosen for the metallographic inspection by scanning electron microscopy (SEM).

The mechanical behavior of the formed parts was characterized by uniaxial tensile tests using a Hegewald & Peschke screw driven tensile testing machine (force capacity: 100 kN) with an extensometer attached directly to the gauge length (**Figure 4a**). The tensile samples were machined by electrical discharge machining in the form of two different geometries, a new tapered and a standard one, as shown in **Figure 4d**. Both tapered and standard samples were taken from the top hat sections.

**Table 1.** Chemical composition of the investigated alloys determined by optical emission spectroscopy.

Chemical elements [wt%]	C	Si	Mn	P	S	Al	Others
22MnB5	0.2–0.25	0.015–0.35	1.10–1.40	0.025	≤0.008	0.015	Ti max. 0.05 B max. 0.005

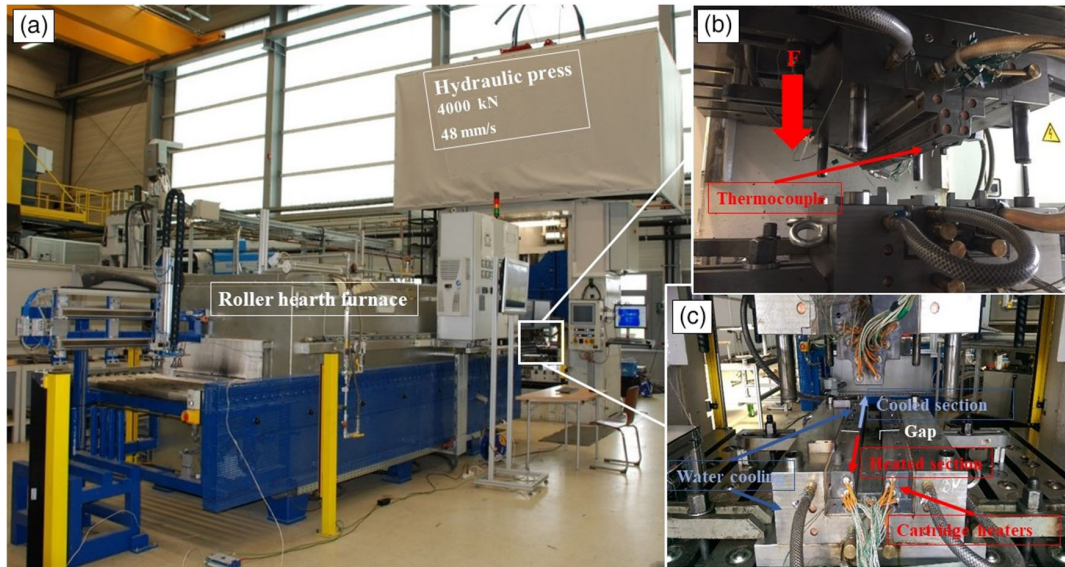


**Figure 2.** Photographs including description of details of the integrated experimental setup for the thermomechanical process route accomplished, including a) a roller hearth furnace and a hydraulic press and the b,c) used forming tools. The upper forming tool (b) is equipped with force transducers and integrated thermocouples to track the force–displacement behavior and measure the sheet temperature during forming operation. The detailed representation in (c) shows the lower forming tool equipped with cooling channels and cartridge heaters. Both (b) upper and (c) lower forming tool consist of a heated and a cooled section, thermally separated by a small gap. The same setup can be used for forming of other alloys such as aluminum alloys as well.<sup>[79]</sup> Reproduced with permission.<sup>[79]</sup> © 2020, WILEY-VCH Verlag GmbH.

**Table 2.** Process parameters selected for the different process routes.

Variant/process parameter set	Austenitization temperature [°C]	Soaking time [s]	Tool <sub>heated</sub> temperature [°C]	Tool <sub>cooled</sub> temperature [°C]	Cooling time within the tools [s]	Microstructure
1	–		As received material			Ferrite/pearlite
2	870	90	18	18	10	Martensite
3	870	90	500	18	10	Graded
4	870	90		Air cooling		Ferrite/pearlite

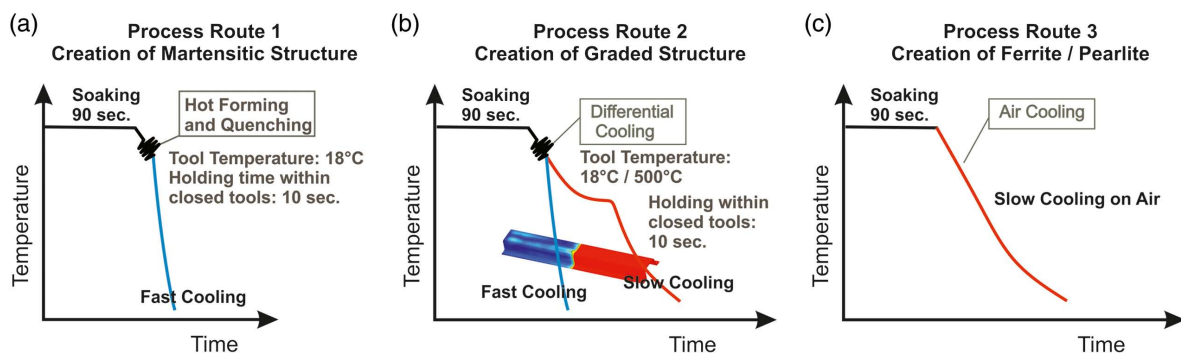


**Figure 3.** Schematic illustration of the investigated thermomechanical process route in this study realized by the experimental setup. a) Process route to obtain fully martensitic structure by cooling within tools at 18 °C after austenitization at 870 °C. b) Creation of graded microstructure by locally different cooling rates due to the differentially tempered tool of 500 and 18 °C. The holding time within closed tools was set to 10 s for both routes. c) Process route of the samples cooled on air to obtain ferritic–pearlitic microstructure.

The tapered geometry was chosen according to the experiences of Eller et al.<sup>[31]</sup> with the aim to center the area of deformation of the functionally graded sample to the transition zone. To guarantee the comparability of the results, the same geometry was used for

the homogenous samples. The standard geometry was selected to identify the location of the initiation of deformation and the change in the corresponding spot in case of nonhomogeneous mechanical properties. For both geometries, a gauge length of

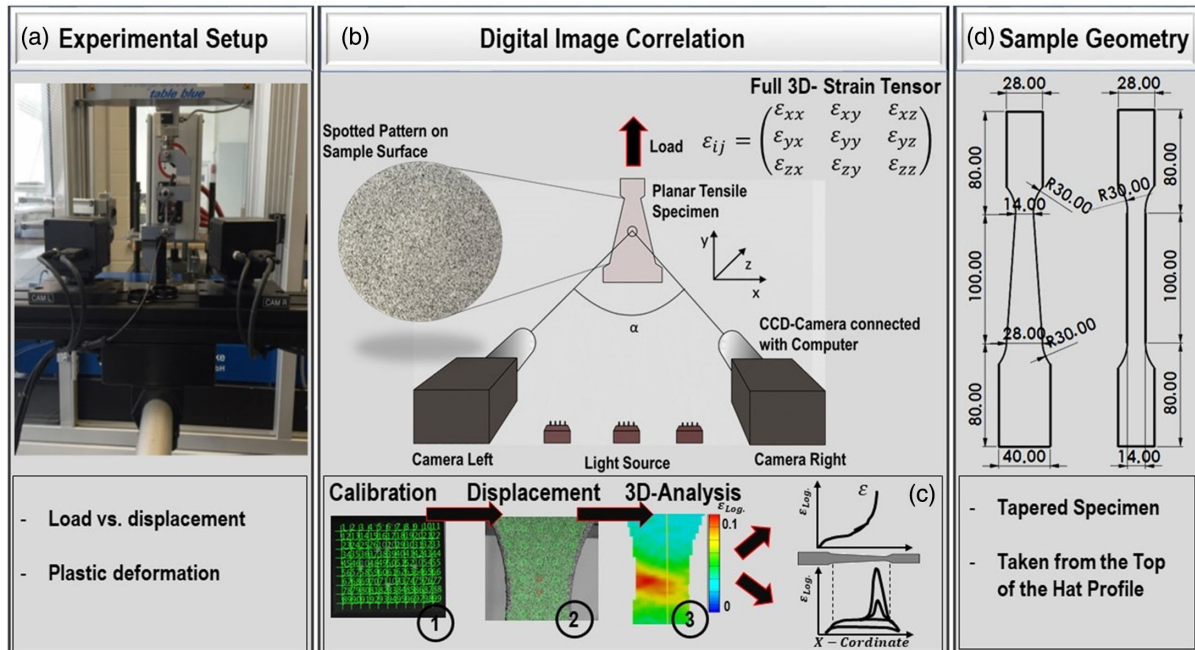


**Figure 4.** Experimental setup and property characterization using a) tensile tests coupled with a DIC system for analysis of both tensile geometries, i.e., tapered and standard. b) Detailed and schematic illustration of the test setup during tensile test showing the prepared surface of the specimen, two CCD cameras focused from different angles on the specimen surface and light sources. c) The procedure of the noncontact local strain measurement from calibration to obtained 3D strain maps and the resulted macroscopic deformation along the specimen surface. d) Used sample geometry in the underlying study.

100 mm was chosen and a minimal gauge width of 14 mm at a sheet thickness of 1.5 mm. The gauge width for the tapered geometry ranges from minimum 14 mm to maximum 28 mm (Figure 4d). All tensile tests were carried out at a crosshead speed of  $5 \text{ mm min}^{-1}$ . The error bars and the standard deviation were calculated by the mean value of at least five measurements.

To characterize any effect related to changes in geometry and stress distribution seen in the local deformation behavior, DIC measurements were coupled with the tensile tests. For this reason, a high contrast surface pattern was created by two different colors sprayed onto the tensile specimen surface (Figure 4). White color provided for a homogeneous uniform white background and black color was used to apply a speckle pattern on the same surface enabling the recording of deformation pattern. It has to be noted that before pattern application, the Al-Si coating was removed from the surface. For image acquisition and local strain measurement, two CCD cameras (Schneider Kreuznach Xenoplan 2.8/50-0511 with a resolution of  $1280 \times 1024$  pixel) were focused from different angles on the same zone of the sample, recording the sample surface at rate of 5 Hz. The focal length of the camera is 50 mm, which covers an image circle of 24 mm with a resolution of  $3.6 \mu\text{m}$ . The calculation of strains from these images was performed by ARAMIS software (GOM—Gesellschaft für Optische Messtechnik mbH, Germany). The corresponding facet sizes for the calculation were set at  $15 \times 14$  for all measurements. It should be noted that for each condition at least three repetitions of DIC measurements were performed to ensure and provide evidence of the reproducibility of the obtained results. The 3D measurement

process steps from 1) calibration using a calibration object for assessing dimensional accuracy, 2) displacement and adjustment of facet sizes for the calculation of 3) the deformation map and the final strain distribution are shown in Figure 4c.

Microstructural evolution was characterized using a high-resolution SEM (Zeiss ULTRA GEMINI, Germany). Standard mechanical grinding and polishing procedures were used to prepare samples for microstructural analysis.<sup>[52]</sup> In addition to the SEM investigations, a high-resolution digital microscope, DSX1000 Olympus, was used to show the obtained microstructure and different phases after the thermomechanical process.

## 3. Results

### 3.1. Microstructure Characterization

Microstructural characteristics as revealed by SEM observations of the investigated samples are shown in Figure 5. The as-received material shows a homogeneous distribution of ferritic–pearlitic grains, Figure 5a, which has been shown numerous in the literature.<sup>[53]</sup> The microstructure of the blank quenched in the cooled tool section, Figure 5b, consists of a fully martensitic structure. This is a clear evidence for the high cooling rate imposed by the forming step.<sup>[53]</sup> In case of SEM analysis of the transition zone of the differentially cooled, microstructurally graded blank, a complex microstructure consisting of ferrite–pearlite and martensite as well as bainite can be observed (Figure 5c). However, here it has to be noted that the locally

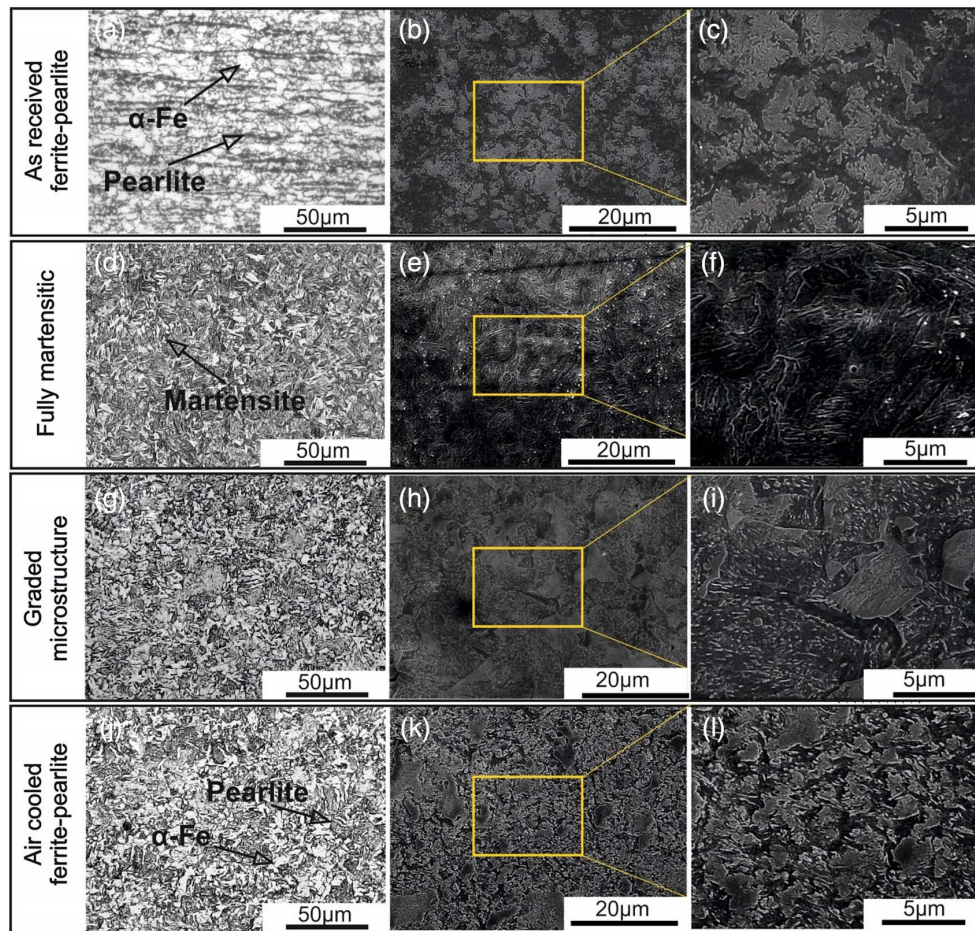


**Figure 5.** Characteristic microstructures for the process routes in focus; investigated microstructure using a,d,g,i) light-optical microscopy and b,c,e,f,h,i, k,l) SEM. The initial as-received microstructure (a–c) consists of homogeneously distributed ferritic–pearlitic grains. The hot formed microstructure using cooled forming tools (d–f) shows predominantly lath martensitic structure due to the high cooling rate explaining the high material strength. The transition zone of the formed structure using the differential cooling technique is shown in (g–i) revealing a complex mixed microstructure, presumably consisting of ferrite–pearlite and martensite as well as bainite. The air cooled microstructure (j–l) after austenitization consists of ferritic and pearlitic structures.

prevailing fractions of these phases may differ. Furthermore, SEM as conducted in current work only is able to provide for a rough qualitative analysis of prevailing phases. For in-depth characterization of such kind of complex microstructure, phase analysis by X-ray diffraction combined with transmission electron microscopy has to be conducted. However, such kind of analysis is beyond the scope of current work and, thus, will have to be considered in future studies. After austenitization followed by air cooling, Figure 5d, the sample is characterized by a slightly finer ferritic–pearlitic microstructure as compared with the as-received material.

### 3.2. Hardness Measurements and Mechanical Properties

Figure 6a shows the hardness measurements of all samples, all being in good agreement with the aforementioned SEM micrographs for the different conditions (Figure 5). The ferritic–pearlitic microstructure of the as-received material is

characterized by a mean hardness value of 186 HV10. The finer structure of the air-cooled sample already shows a slightly higher mean value of 240 HV10, whereas the martensite being present upon tool quenching increases the hardness level up to 495 HV10. The hardness profile along the complete graded sample shows an increase from 237 to 417 HV10, in the transition zone between 200 and 300 mm, chosen as gauge length (coordinates in relation to the initial blank) increases the hardness from 250 to 280 HV10. The hardness profile clearly reveals the gradual change in local microstructure from ferrite–pearlite to martensite. The area characterized by the characteristic hardness increase was chosen for the following tensile tests.

The in situ tensile tests (using the coupled DIC system) conducted in this study for the different microstructures (established by the four process routes considered) were used to determine the global elongation  $\Delta L$  with respect to the initial length  $L_0$ . At the same time, the maximum load during plastic deformation was analyzed (Figure 6b). Obviously, the maximum tensile load of the graded structures is located between the level of

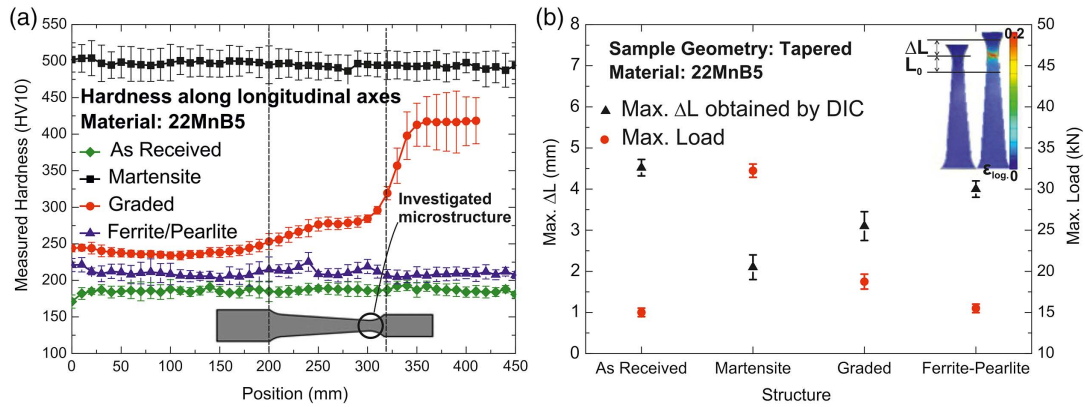


**Figure 6.** a) Hardness profiles of the investigated material conditions following different process routes. The black line shows the fully martensitic structure with highest hardness level, the red line the graded structure after differential cooling, the blue line the ferritic/pearlitic structure, and the green line the as-received condition. The inset depicted in (a) shows the tapered sample geometry and its position within the formed initial sheet (with respect to the hardness gradient) including the sample area where micrographs shown in Figure 5 were recorded. b) Load and displacement for different microstructure conditions. As the selected specimen geometry for the tensile tests does not allow for the geometrical calculation of the ultimate tensile strength, the maximum tensile load (max. load) obtained by the tensile testing machine is shown in this diagram to give a better sense of the material strength.  $\Delta L$ , moreover, in figure presents the obtained total elongation (mm) after tensile tests for each condition.

the soft ferrite–pearlite and hard martensite conditions at an intermediate stage (Figure 6b). This behavior is due to the mixed microstructure, as indicated by the SEM results in Figure 5. The corresponding formability, characterized by the global elongation  $\Delta L$ , of the different microstructural states reflects the inverse trends with respect to strength and ductility. As a consequence, the lowest elongation was obtained for martensite, the highest for the ferritic–pearlitic microstructure. In direct comparison, highest ductility was found for the as-received ferrite–pearlite material, which was even higher than for the air-cooled sample being characterized by the presence of the same phases, however a slightly finer microstructure. Concerning the load and deformation behavior of the graded structure, a relatively high plastic deformation in combination with a relatively high strength is seen.

### 3.3. Microscopic Deformation Behavior Using the Tapered Sample Geometry

The macroscopic deformation behavior of all microstructural conditions is represented by the progression of the logarithmic strain up to failure and the corresponding local deformation maps in tensile direction (Figure 7). The strains, obtained from the 3D DIC system, are the average of Green–Lagrange strains concerning the relationship between the reference undeformed tensile sample and the deformed sample after loading.<sup>[54]</sup> In scientific studies dealing with the DIC technique, the strain after plastic deformation commonly is given as logarithmic strain. Therefore, the average of Green–Lagrange strains are converted into the logarithmic strain defined by the following definition along the sample cross section<sup>[55]</sup>

$$\epsilon_{yy} = \frac{1}{2} \ln(1 + 2\bar{E}_{yy}) \quad (1)$$

where  $\epsilon_{yy}$  is the logarithmic strain,  $\bar{E}_{yy}$  is the average Green–Lagrange strain obtained by the relation between the images

of deformed and undeformed state, and  $y$  represents the longitudinal direction of the strain. In the following in all figures of this study, the strain, obtained by the DIC technique, consequently represents, in line with many other studies, the logarithmic strain.

Plastic deformation appears mainly very locally, i.e., in the sample section being characterized by reduced width. This behavior is intentionally enforced by the tapered geometry. Figure 7a shows the logarithmic strain evolution for the as-received material. Already in the very early stages of deformation, homogeneous plastic deformation is seen, with this characteristic prevailing up to the necking point. After necking, high local deformation with absolute values up to  $\epsilon_{\text{true}} = 0.49$  and a distinct reduction in the area are seen, being a clear indication for the high ductility of this material condition. A similar strain map is observed for the ferritic–pearlitic material of the austenitized and air-cooled sample (Figure 7d). However, the magnitude of the strain field shortly before failure is significantly lower ( $\epsilon_{\text{true}} = 0.34$ ). Only limited plastic deformation is seen within the area of interest of the fully martensitic microstructure, Figure 7b, clearly representing the high hardness and low formability. The plastic strain occurring after the necking point resembles the shape of a deformation band with an angle of almost  $50^\circ$  to the tensile direction, however without any traces of further propagation along the sample surface or plastic instability. Still, a relatively high local deformation level after necking of  $\epsilon_{\text{true}} = 0.27$  is seen. A schematic illustration of the shear band angle determination is shown in Figure 8f.

The progression of the local strain until failure of the graded material shows some special features as compared with the homogenous samples (Figure 7c). Initially, i.e., before necking, the corresponding profile along the tensile axis obtained by DIC reveals a homogeneous deformation in the area of interest. Directly after the necking point, pronounced plastic strain localization is seen, which occurs interestingly in the form of two crossed deformation bands. When further plastic deformation



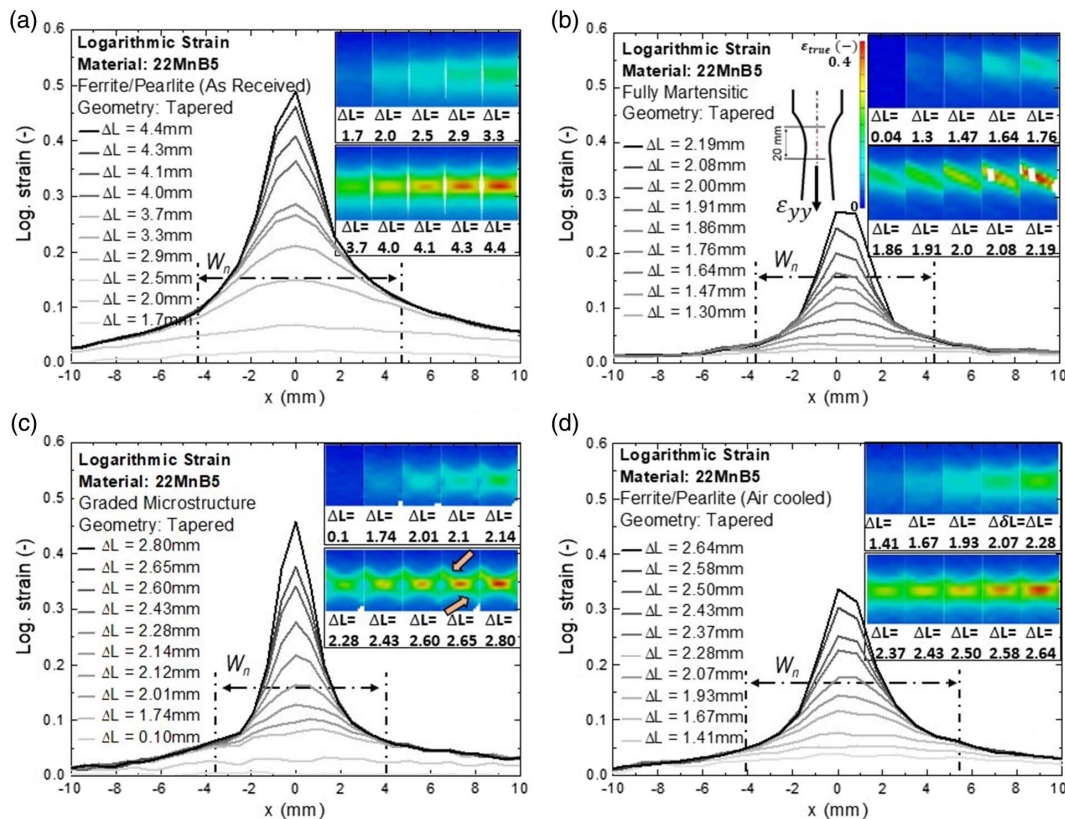


**Figure 7.** Local deformation behavior and the corresponding deformation profile maps along the tensile direction in the investigated area on the sample surface of all conditions during straining: a) as-received, b) fully martensitic, c) microstructurally graded, and d) air-cooled samples. The deformation profiles represent the studied zone (20 mm) along the tensile axis. Orange arrows in (c) show double shear bands for the graded microstructure.  $W_n$  (mm) indicates the width of the first strain localization resp. neck width.

under continuous increase in the tensile load is promoted, only minor changes are directly seen. The angle between the nucleated bands and the  $\epsilon_{yy}$  direction is almost  $50^\circ$ . A strong concentration in the intersection zone of the two bands (see orange arrows in Figure 7c) can be observed, which leads to a very high localized deformation of about  $\epsilon_{true} = 0.45$ , even in this hardened condition. Obviously, this value obtained is close to the maximum strain of the as-received sample. However, plastic strain prevails only in a more localized necking area and eventually a lower global displacement  $\Delta L$  results. Moreover, the width of neck ( $W_n$ ) after plastic deformation is also marked in Figure 7a–d for all material conditions. The highest width of neck (9 mm) was observed for the air-cooled material.

### 3.4. Macroscopic Deformation Behavior of Graded Samples Characterized Using a Standard Tensile Geometry

To eliminate the geometry influence on the allocation of the deformation area, the graded specimens were also investigated using a straight standard sample geometry for tensile testing. The local deformation maps and the course of local strain progression to failure are complemented with hardness profiles measured before and after the tensile tests (Figure 8). Interestingly, two different local deformation behaviors in case of the standard tensile

specimens can be revealed using the DIC technique during the tensile test. In the first case, up to the point of necking a large zone within the gauge length (from 10 to 117 mm) being characterized by homogeneous deformation is observed (Figure 8b). The hardness measurements after tensile testing as compared with those before the test support the DIC observation, where an increase in the hardness level of this zone is detected, leading to a kind of leveling of the properties (Figure 8a). Immediately after first neck initiation, the localized plastic deformation in the harder region can be seen. DIC results indicate clearly the nucleation of a single shear band in the softer zone of the tensile specimen after the necking point (Figure 8b). This phenomenon shows a fixed angle ranging from  $48^\circ$  to  $52^\circ$  with respect to tensile direction ( $\epsilon_{yy}$ ). Similar to the tapered geometry, this kind of shear localization process occurs prior to the fracture incidence. It is worth noting that only in case of the tapered geometry, a double shear band was observed for the graded sample. Due to this fact, the resulting local strain before failure of the standard geometry is thought to be lower ( $\epsilon_{true} = 0.36$ ).

In the second case, first homogenous deformation along the specimen up to the necking point is seen. This behavior resembles the evolution detailed for the previous case. However, with increasing the plastic strain, multiple necking sites at two different spots occur as can be clearly identified on the sample surface

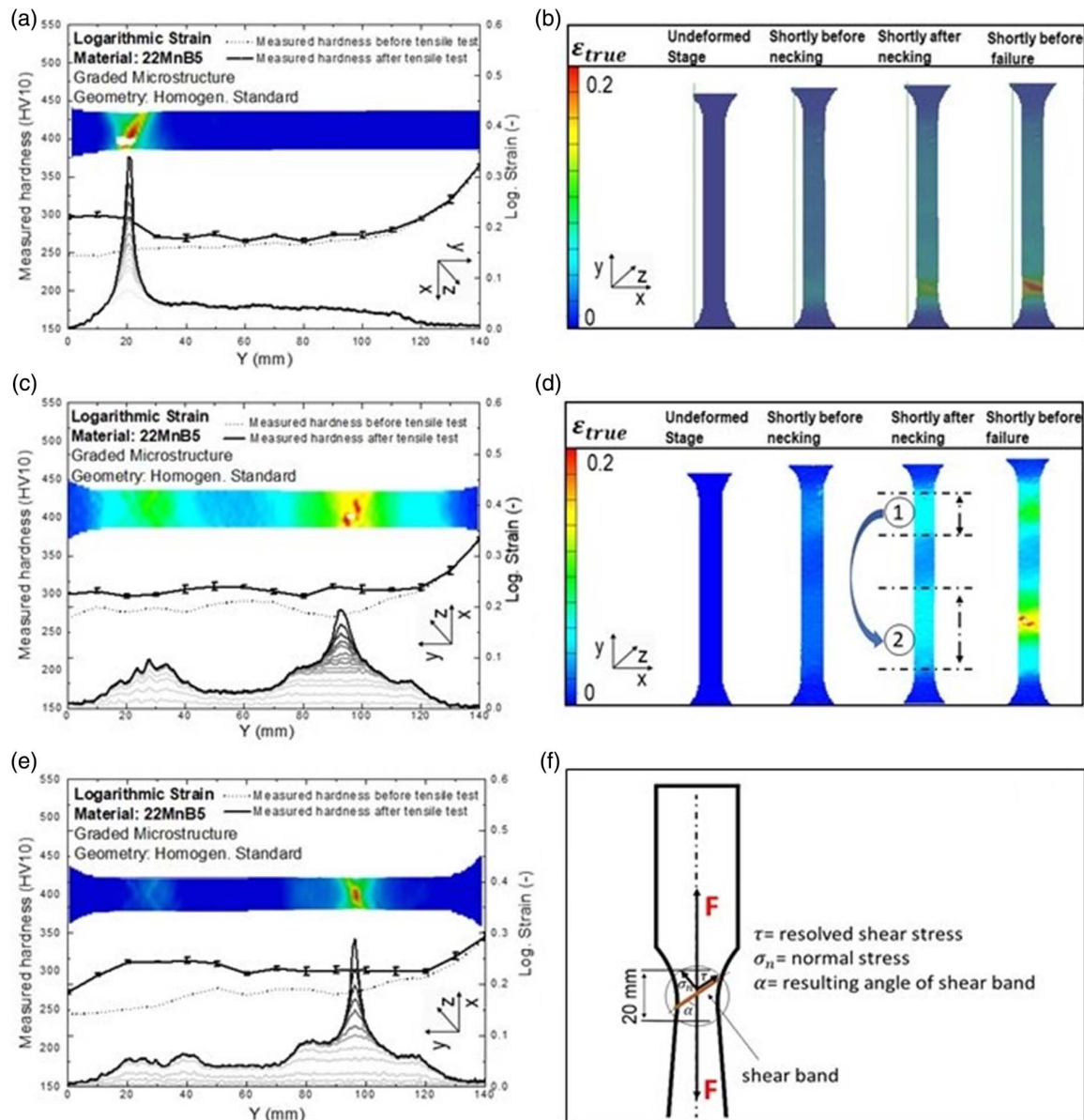


**Figure 8.** Local deformation behavior and 3D deformation map of microstructurally graded standard tensile samples indicating different deformation behavior. a) The local deformation profile of the graded structure using the standard sample geometry showing an increase in the logarithmic strain in the soft zone and the appearance of only a single deformation localization area. The corresponding hardness profile after the tensile test represents an increase in material strength mainly in the neck zone. b) 3D deformation map further confirms the observed plastic deformation behavior and the appearance of only a single neck on the tensile specimen. c) The local deformation profile of the graded structure shows multiple necking sites at two different spots up to failure and d) the 3D deformation map at different deformation stages shows the length and the position of both necking zones. e) Another tensile sample reveals the strain localization at different regions. f) Schematic illustration details the shear band angle determination.

by evaluating the DIC results. According to the hardness profile before tensile testing, neck nucleation occurs in two zones indicated as soft. This happens almost at the same time in both regions, labeled 1 and 2 (Figure 8d). Initially, the localization of strain is more pronounced in region 1 of the specimen. Interestingly, with increasing the plastic strain and tensile stress, neck propagation in region 2 dominates and the failure occurs mainly in this region. This phenomenon has been observed in several tests.

### 3.5. Fractography

To analyze the underlying fracture mechanisms during the tensile tests, selected samples were further investigated by SEM. The fracture surfaces of both as-received and air-cooled samples are characterized by large dimple-like facets being a clear indication of ductile failure (Figure 9). The fracture surface of the fully martensitic sample demonstrates small-sized and shallow dimples as compared with that of the ferrite–pearlite ones. These

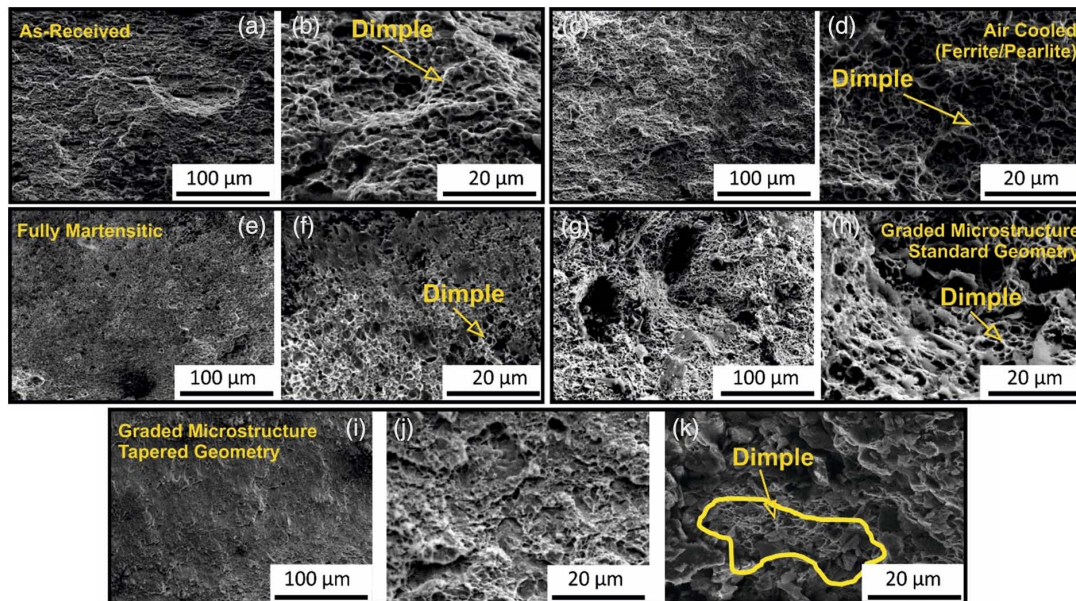


**Figure 9.** Fracture surfaces of samples upon the tensile testing: a,b) the initial as-received sample consisting of ferritic and pearlitic structure, c,d) the air cooled sample consisting of ferritic and pearlitic structure after austenitization), e,f) the hot formed samples cooled in forming tool with predominantly lath martensitic structure, and i–k) the sample with a complex mixed microstructure depicted from the transition zone of the formed structure using differential cooling technique. Both a,c,e,g,i) low and b,d,f,h,j,k) high magnifications are demonstrated. In (k), a region containing of dimple features is indicated by the yellow line.

differences already can be considered as an indication that as-received and air-cooled samples should show better ductility during plastic deformation as a larger portion of deformation prevails before final failure. In the case of the graded microstructure, ductile and dimple-like facets are evident in case of the standard sample geometry, while the fracture surface of the tapered sample shows a mixture of two different fracture morphologies, i.e., deep and shallow dimples. Moreover, dimples are indicated for all conditions by yellow arrows on the fracture surfaces. The sizes of dimples are measured to be around 10 and 5  $\mu\text{m}$  for the ferrite–pearlite and fully martensite samples, respectively. The sizes of dimples for the graded samples vary from 5 to 10  $\mu\text{m}$ , indicating the presence of different phases on the fracture surfaces.

## 4. Discussion

### 4.1. Influence of Microstructure on Local Deformation Behavior

Based on the strain measurements, extensive necking of the ferritic–pearlitic microstructure in the as-received condition can be seen as plastic deformation progresses. The neck width  $W_n$  is about 9 mm and shows a maximum logarithmic strain of  $\epsilon_{\text{true}} = 0.5$  (see Figure 7a). The tensile test results in a maximum load of 15 kN and the highest maximum displacement of  $\approx 4.52$  mm (Figure 6b). The observed fracture surfaces indicate a ductile material failure appeared for the as-received material. During the tensile test, the maximum equivalent stress is parallel to the direction of the load; therefore, fracture of the specimen appears at an angle of  $90^\circ$  to the tensile force  $F$ . On the

microstructural level, this can be explained by the behavior that small cavities or micropores developed due to the applied load shortly after the first neck initiation. It was previously reported that the growth and coalescence of voids stem from strain localization during internal necking.<sup>[55,56]</sup> As the load level increases, the size of cavities increases and eventually they merge and form an elliptical crack with a longitudinal axis perpendicular to the direction of loading (Figure 10a). During the tensile test, the maximum equivalent stress is parallel to the direction of the load; therefore, based on the mentioned criterion, fracture of the specimen appears at an angle of  $90^\circ$  to the tensile force  $F$ .

The obtained tensile test results of the martensitic specimens in this study revealed, on the one hand, very high material strength up to 32.5 kN and, on the other hand, very low displacement of 2.08 mm (Figure 6b). Accordingly, this structure shows a brittle behavior with poor plastic deformation, which can be seen in the corresponding local deformation map (Figure 7b) and the fractography analysis (Figure 9). Due to these findings, the martensitic microstructure has the lowest local and global strain  $\epsilon_{\text{true}} = 0.29$  with a neck width  $W_n$  of 7.2 mm. In addition to these observations, the DIC images documented that the tensile specimen fails due to shear fracture at an angle of  $66^\circ$ . The maximum shear stress occurs at an angle of  $45^\circ$  relative to the direction of normal stress. Figure 10b shows schematically the crack initiation and growth of the martensitic tapered tensile specimen until complete failure. The crack nucleation and propagation in martensitic structures are strongly affected by the martensite needle boundaries and their morphology.<sup>[57,58]</sup> Moreover, in martensitic structures, microfailure occurs generally in sharp corners on martensitic boundaries in a place of high stress concentration.<sup>[59]</sup> The formation and propagation of high number of microcracks

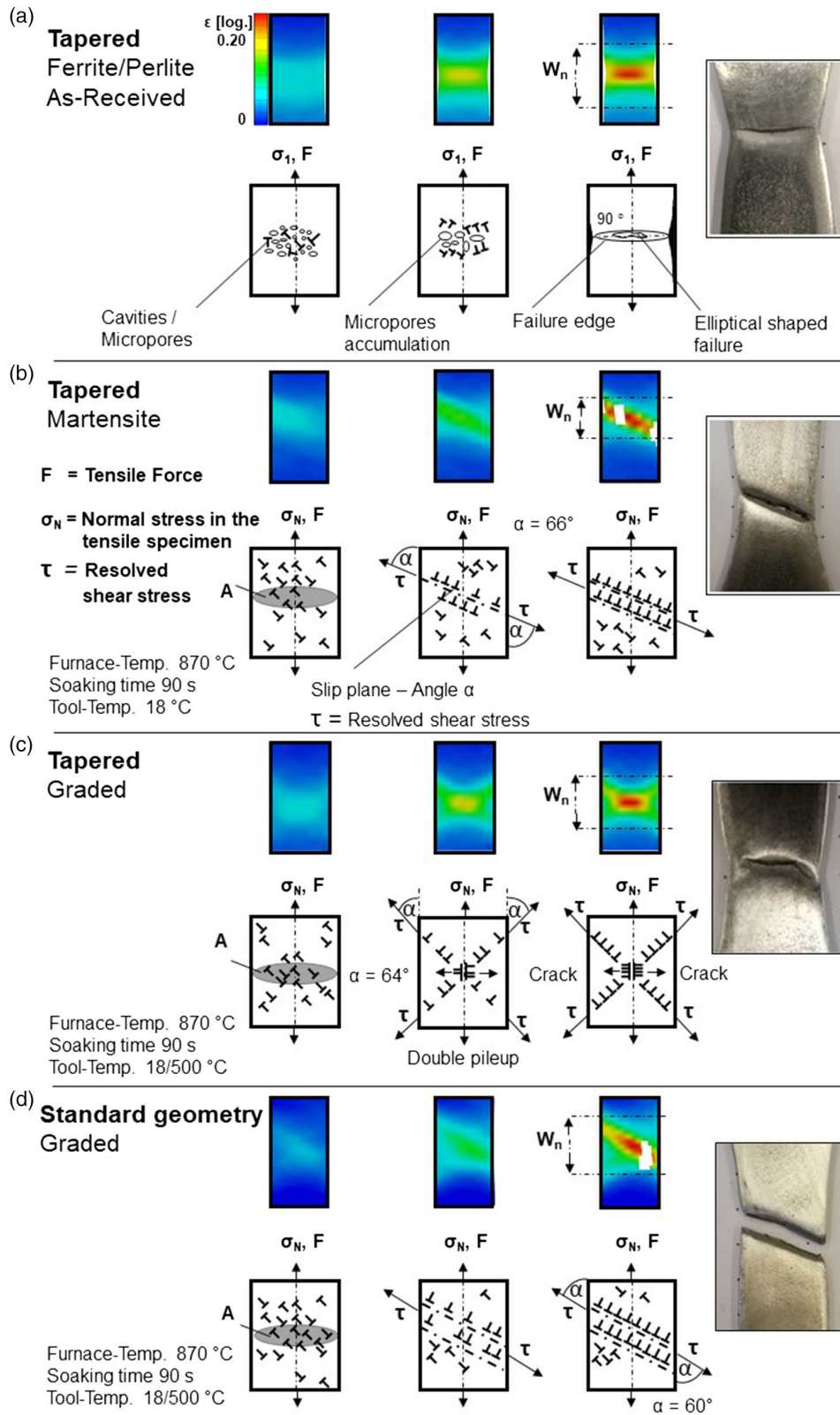


**Figure 10.** Elementary mechanisms contributing to final failure for all conditions considered: a) as-received, b) fully martensitic, c) tapered, and d) standard sample geometry used for characterization of the microstructurally graded structure.

due to the high number of martensite interfaces eventually further lead to plastic instability during straining, influencing the shear band orientation. However, the deviation between the experimentally determined angle of  $66^\circ$  and the theoretical maximum shear stress occurring at an angle of  $45^\circ$  could be caused by a predamage of the material structure, the crystallographic orientation of grains in the deformed zones as well as the stress concentration due to the tapered tensile specimen geometry.<sup>[59–62]</sup> Such deviation is also reported elsewhere in the literature for different materials.<sup>[63–65]</sup> Renard et al. showed in their study on TWIP steel an angle between the band direction and the tensile axis of  $54^\circ$  measured using DIC technique.<sup>[63]</sup> A prediction of the shear band angle under tensile load, which was carried out by Hill et al., results in an angle of  $53^\circ$ .<sup>[65]</sup> Further experimental investigations focusing on the kinematics fields and spatial activity of Portevin–Le Chatelier (PLC) bands of an Al–4.5% Mg (wt%) alloy revealed band angles ranging from  $53^\circ$  to  $64^\circ$  with respect to the tensile axis.<sup>[66]</sup> Grains are able to align to the direction of stress in tensile test with respect to their orientation at high strains as has been shown theoretically and experimentally.<sup>[67]</sup> A detailed theoretical investigation on the texture evolution is also conducted by Jia et al.<sup>[67–70]</sup> Anyhow, the aforementioned deformation evolution and failure behavior are in good agreement with expected common observations for those microstructures.<sup>[71,72]</sup>

The strain maps obtained by using DIC technique show for the functionally graded microstructure a different hardening behavior. Due to the enhanced ductility of the graded resp. mixed microstructure compared with the martensitic structure, the neck width  $W_n$  increases up to 8.3 mm. Furthermore, the maximum true strain rises by 20% ( $\epsilon_{\text{true}} = 0.4$ ). The local deformation after necking appears for this condition by means of two crossed deformation bands at an angle of  $64^\circ$ , whereas for the as-received and air-cooled materials a homogeneous plastic deformation and distinct reduction in the area was found (Figure 7). For the graded microstructure, an apparent homogeneous local strain distribution is observed at the beginning of the experiment in the center of the sample, which could be the trigger or nucleation site for the crossed bands. As plastic deformation proceeds upon increasing the global stress, dislocation interaction and multiplication promote strain localization under oblique angles. Resulting microstructural features finally penetrate multiple crystals in different directions.<sup>[34,68]</sup> Moreover, the mixed microstructure consisting of various phases with different physical properties and slip systems could lead to multiaxial stress states forming two deformation band with dissimilar orientations. As highlighted in the literature, the phases prevailing in steels are characterized by different stress absorptions.<sup>[34,36,58]</sup> In Tazan et al.'s investigations, the local stress map obtained by crystal plasticity simulation is presented for DP steels. It is clearly shown that the martensite is carrying more applied stress compared with ferritic grains.<sup>[32]</sup> Assuming the scenario that moving dislocations cannot leave their slip plane and are piled up at an obstacle, e.g., in the form of a grain boundary, dramatically high stress can result inside the material. With increasing the plastic deformation, the shear bands grow and become more diffused. This behavior is caused by the deformation zones of highly concentrated plastic flow, which are frequently observed at high deformation levels as well for other materials.<sup>[69]</sup> Therefore,

the occurrence of deformation induced crossed shear band can be linked to the heavily deformed zones of the material.<sup>[68,73]</sup> Moreover, the almost symmetric increase in the local strain during tensile test, Figure 6c, confirms the continuous and simultaneous increase in local strain of both deformation band at different orientation and location.

Figure 10c shows the damage behavior of the graded material with a tapered tensile specimen geometry. A prerequisite for the formation of a fracture nucleus is stress concentration locally in the material or on its surface, higher than the global stress  $\sigma$ . Depending on the crystallographic orientation of the soft phase grains, a double-sided accumulation may appear and results in a high-stress concentration. Here, the high stress, significantly higher than the average, eventually leads to very high localized strains and finally the microstructural evolution detailed in the article. Moreover, a high microscopic stress can appear due to the morphology changes and different phases in the material. These phenomena are commonly known from DP steels.<sup>[74]</sup> This induces the growth and coalescence of microcavities and microcracks in a very restricted area and promotes crack growth transverse to the direction of loading.<sup>[75]</sup>

#### 4.2. Influence of Sample Geometries on Local Deformation Behavior of Graded Samples

A more interesting deformation behavior is observed for the functionally graded samples with a microstructure consisting of gradually changing fractions of ferrite–pearlite, bainite, and martensite. According to Eller et al., in the course of their development of a constitutive material model it is supposed to be a mixture of the forming behavior of the single-phase fractions.<sup>[30,31]</sup> To validate their model for functionally graded 22MnB5, and to analyze mechanical properties and the failure behavior of samples, featuring a hardness transition in the gauge section, they chose a particular tapered tensile sample geometry to control the area of deformation and failure avoiding a trivial solution. They supposed that failure will always happen in the initial softest zone, supposedly the area with the highest amount of ferrite–pearlite. Therefore, different gauge widths should force the failure location to zones of higher hardness. By varying the minimal width, different failure locations were obtained representing different amounts of harder phases. But interestingly with a sample geometry with a lower difference between maximum and minimum width a deviation between the simulated and experimental failure location was found. Also, the simulation revealed shortly before failure two deformation zones which were not reported for the experimentally obtained via DIC results. Therefore, it seems that complex strain hardening and deformation behavior of the multiphase microstructures will not be adequately represented by tapered samples only. Based on their investigations mentioned earlier, tapered and nontapered specimen geometries were comparatively used in the current study to minimize a possible influence of the geometry and to identify the influence of microstructure on the localization of deformation, the overall deformation behavior as well as on a change in failure mechanisms.

In case of the deformation behavior of the graded material, the DIC deformation map shows the occurrence of two opposing

shear bands at an angle of  $64^\circ$  during plastic deformation with a tapered tensile specimen geometry. This behavior may eventually be attributed to the interaction of a mixed microstructure and a multiaxial stress state caused by the tapered geometry. Due to the enhanced ductility of the graded resp. mixed microstructure compared with a martensitic structure, the neck width  $W_n$  increases up to 7.8 mm (Figure 7c). Furthermore, the maximum true strain rises up to  $\epsilon_{\text{true}} = 0.4$  compared with that of the martensitic structure. When changing to a standard tensile geometry, the DIC strain map displays a failure under shear stress at an angle of  $60^\circ$  for the sample with graded mixed microstructure (Figure 10d). The obtained neck width is with  $W_n = 15.2$  mm higher than the one of the tapered sample geometries. As both samples consist of the same mixed microstructure, the influence of the testing geometry is obvious. The constant increase in the cross section along the longitudinal axis of the tapered tensile specimens localizes the plastic deformation and the necking of the material to a specific area which creates also the multiaxial stress state.<sup>[63,76]</sup> In case of the standard tensile specimen, this forced localization is avoided, and the appearance of shear bands is more random. Therefore, only one shear band appears in the cross-sectional zone depending on the more random appearance of softer areas within the mixed microstructure (Figure 10d).

### 4.3. Elementary Findings Based on Experimental Results on Graded Samples

The analysis of the local deformation behavior of 22MnB5 samples using DIC technique during uniaxial tensile test reveals the nonuniform distribution of plastic deformation of different microstructures. DIC technique has been used in a great number of scientific works to investigate and measure geometrical changes.<sup>[48,49,76]</sup> Despite the limitations, this technique involves a high potential for the use in several scientific fields.<sup>[50,77]</sup> Although this method depends on a proper understanding of the physical material mechanisms to interpret the local strain fields, this method can identify characteristic differences depending on the microstructural features, which are not detected by common testing methods. However, the spatial distribution of logarithmic strain represents different types of localized failure along the gauge section after necking, which appear depending on the microstructure and strain distribution as shear bands, crossed bands, or homogenous local strain at the failure region. In case of the graded sample with standard geometry, less local strain and complex failure behavior are observed. Accordingly, the mechanical response of the obtained mixed microstructure after thermomechanical processing is governed by the macroscopic stress and strain partitioning behavior clearly shown by the DIC measurements. This specific behavior is triggered due to different existing phases and depends on the evolution of local strain and stress. Among the experimental observations in this study, the strain mapping of tensile specimen shows more or less a random necking behavior. Regarding these phenomena, the hardening behavior, damage nucleation, and dislocation density gradient with the mixed microstructure should be taken into account for explaining the necking behavior.<sup>[32]</sup>

In general, necking in materials is caused by a high degree of strain localization over a particular zone of the specimen after

uniform deformation.<sup>[78]</sup> In adequate conditions, the neck zone undergoes pronounced local strain hardening as plastic deformation increases and becomes stronger than the neighboring regions. This behavior is able to promote a shifting of the neck zone toward softer neighboring regions as seen here in the second case for the standard sample geometry. Due to this phenomenon, the load-carrying capacity of the tensile geometry as well as the elongation at fracture increases. Tensile tests coupled with DIC measurements on graded structures in this study reveal that before the appearance of strain localization, a slight leveling of flow stress seems to happen in the beginning of deformation leading to an initial almost homogenous plastic strain distribution despite the inhomogeneous microstructure. The supposed slightly higher strain rate in initial softer areas leads to some amount of strain hardening, increasing the soft areas strength. Hardness profiles before and after the tensional straining confirm this observation (Figure 8c). A more complex deformation behavior with multiple necking at several sites at less local strain was therefore found for the graded microstructures with the help of standard tensile geometry. This leads to the conclusion that the mixed microstructure accumulates more plastic strain during plastic deformation in case of the occurrence of multiple necking when using the standard geometry. Moreover, based on the DIC results, the type of the neck of the material can be related to microstructure and geometry dependence. Therefore, it should be noted that failure does not occur with complete certainty in soft zones of the graded structures set by the thermomechanical forming process, but also the complex deformation behavior and the strain hardening of different phases are important influences. Mechanical properties, underlying microstructural, and failure mechanisms of graded materials are still under investigation and are not fully understood. Thus, more in-depth analysis of microstructure during deformation is needed to establish property–microstructure–damage relationship. This will be addressed in a follow-up study.

## 5. Conclusion

In the current study, various forming strategies were used utilizing segmented, differentially tempered forming tools to tailor the local microstructures of 22MnB5 to obtain different characteristic monolithic (ferritic–pearlitic as well as martensitic) and functionally graded microstructures. DIC coupled with tensile tests was applied to evaluate and differentiate the properties of functionally graded components. Tests with tapered geometries were compared with those with nontapered sample geometries to gain insights into the influence of sample geometries on the obtained results. From the results obtained, the following conclusions can be drawn: 1) Based on the DIC measurements it can be deduced that the microstructure of the formed parts influences significantly the deformation behavior of the material. The martensitic as well as graded microstructure revealed higher degrees of strain localization as compared with the as-received and the ferritic–pearlitic structure, respectively. 2) The observed difference between the angle of experimentally obtained shear bands and the theoretically maximum shear stress most likely could be caused by the stress concentration in the tapered geometry. Moreover, the spatial distribution of the logarithmic strain

represents different types of localized failure depending on the sample geometry for the graded material. The complex strain hardening behavior of the graded structure in the transition zone, when using the standard geometry, may lead to the occurrence of multiple necking sites. 3) A mixture of two different fracture morphologies, i.e., deep as well as shallow dimples were found as expected in the tailored samples due to the existence of a mixture of softer and harder phases. Despite the complex deformation and strain hardening behavior, the failure mechanisms of the investigated microstructures may be explained by crack initiation and growth after necking. In-depth analyses of microstructures and dissimilar phases should be conducted to understand well microstructural evolution and failure mechanisms in tailored samples. These investigations are, however, beyond the scope of the current work and should be addressed in a follow-up study. 4) The DIC technique applied was used to establish a proper understanding of elementary mechanisms to eventually interpret the evolution of local strain fields. This enabled the identification, characterization, and evaluation of microstructural differences as well as geometrical features, which cannot be assessed by common testing methods. 5) Further research will be necessary to establish this method especially in the field of testing of materials with property distributions. Concerning the strain localization and different deformation behavior of the investigated microstructure, in situ deformation experiments using high-resolution microscopy as well as crystal plasticity simulations are needed to understand the deformation behavior on the microscale in depth.

## Acknowledgements

The authors thank Mr. Dipl.-Ing. Stefan Seidel and Eduard Fuhrmann for sample preparation.

Open access funding enabled and organized by Projekt DEAL.

## Conflict of Interest

The authors declare no conflict of interest.

## Data Availability Statement

Research data are not shared.

## Keywords

digital image correlation, functional gradation, logarithmic strain, microstructures, thermomechanical processing

Received: November 13, 2020

Revised: March 8, 2021

Published online: April 10, 2021

- [1] K. Steinhoff, in *Proc. 1st Int. Semin. Hot Sheet Met. Form. High-Performance Steel* (Eds: K. Steinhoff, M. Oldenburg, B. Prakash), **2010**, p. 153.

- [2] K. Steinhoff, M. Maikranz-Valentin, U. Weidig, U. Paar, E. Gücker, in *Tagungsband Zum 2. ErlangerWorkshop Warmblechumformung* (Ed: M. Geiger), Meisenbach Verlag **2007**, p. 1.
- [3] K. Steinhoff, H. J. Maier, D. Biermann, *Functionally Graded Materials in Industrial Mass Production*, Vol. 32, Verlag Wissenschaftliche Scripten Kaiserstrasse, Auerbach, Germany **2009**, p. 08209.
- [4] L. Golem, L. Cho, J. G. Speer, K. O. Findley, *Mater. Des.* **2019**, *172*, 107707.
- [5] K. Steinhoff, A. Ademaj, S. Prokoph, M. Schupfer, U. Weidig, in *Erlanger Work, Warmblechumformung* **2012**, p. 85.
- [6] M. Maikranz-Valentin, U. Weidig, U. Schoof, H. Becker, K. Steinhoff, *Steel Res. Int.* **2008**, *79*, 92.
- [7] O. Cavusoglu, O. Cavusoglu, A. G. Yilmazoglu, U. Uzel, H. Aydin, A. Güral, *J. Mater. Res. Technol.* **2020**, *9*, 10901.
- [8] D. Berglund, K. Amundsson, L. O. Hellgren, in *1st Int. Conf. Hot Sheet Met. Form. High-Performance Steel* (Eds: K. Steinhoff, M. Oldenburg, B. Prakash), Bad Harzburg (D): Grips Media GmbH, Kassel **2008**.
- [9] H. gyu Kim, C. Won, S. Choi, M. gyu Gong, J. gyu Park, H. Lee, J. Yoon, *Int. J. Automot. Technol.* **2019**, *20*, 813.
- [10] A. Bardelcik, C. P. Salisbury, S. Winkler, M. A. Wells, M. J. Worswick, *Int. J. Impact Eng.* **2010**, *37*, 694.
- [11] K. Steinhoff, M. Maikranz-Valentin, N. Saba, U. Weidig, in *Herstellung Und Weiterverarbeitung von Flachprodukten* (Ed: R. Kawalla), Freiberg (D), TU Bergakad **2009**, p. 130.
- [12] K. Steinhoff, N. Saba, M. Maikranz-Valentin, U. Weidig, in *Proc. 2nd Int. Conf. Hot Sheet Met. Form. High-Performance Steel* (Eds: K. Steinhoff, M. Oldenburg, B. Prakash), **2009**, p. 29.
- [13] U. Weidig, K. Hübner, K. Steinhoff, *Steel Res. Int.* **2008**, *79*, 59.
- [14] A. Ademaj, A. Donis, U. Weidig, K. Steinhoff, in *4th Int. Conf. Hot Sheet Met. Form. High-Performance Steel*, **2013**, p. 401.
- [15] M. Maikranz-Valentin, N. Saba, U. Weidig, R. Weißner, K. Steinhoff, in *1st Int. Conf. Hot Sheet Met. Form. High-Performance Steel* (Eds: K. Steinhoff, M. Oldenburg, B. Prakash), Grips Media GmbH **2008**, p. 191.
- [16] M. Merklein, T. Stöhr, T. Svec, M. Wieland, *Light. Des.* **2010**, *3*, 52.
- [17] A. Ademaj, U. Weidig, K. Steinhoff, in *Proc. 4th Int. Conf. Hot Sheet Met. Form. High-Performance Steel—CHS2* (Eds: K. Oldenburg, M. Prakash, B. Steinhoff), Luleå (Sweden) **2014**, 239.
- [18] M. Koizumi, in *Ceram. Trans. Funct. Gradient Mater.*, Vol. 34, (Eds: J. B. Holt, M. Koizumi, T. Hirai, Z. A. Munir), American Ceramic Society, Westville **1993**, p. 3.
- [19] M. Johnsson, in *1st Int. Semin. Hot Sheet Met. Form. High-Performance Steel Steel* (Eds: K. Steinhoff, M. Oldenburg, B. Prakash), University of Kassel/Luleå University of Technology, Hannover (D) **2010**, p. 41.
- [20] H. J. Maier, S. Tschumak, U. Weidig, K. Steinhoff, *Steel Res. Int.* **2008**, *79*, 105.
- [21] U. Weidig, N. Saba, K. Steinhoff, *WT-Online* **2007**, *97*, 745.
- [22] K. Steinhoff, in *Neuere Entwicklungen in der Massivumformung* (Eds: M. Liewald, K. Siegert), MAT INFO Werkstoff-Informationsgesellschaft MbH, Frankfurt, America **2005**, 277.
- [23] M. Merklein, J. Lechler, M. Geiger, *CIRP Ann.* **2006**, *55*, 229.
- [24] M. Naderi, A. Saeed-Akbari, W. Bleck, *Mater. Sci. Eng., A* **2008**, *487*, 445.
- [25] M. Schrenk, S. Krenn, M. Rodríguez Ripoll, A. Nevosad, S. Paar, R. Grundtner, G. Rohm, F. Franek, *J. Manuf. Process.* **2016**, *23*, 222.
- [26] A. Bardelcik, M. J. Worswick, S. Winkler, M. A. Wells, *Int. J. Impact Eng.* **2012**, *50*, 49.
- [27] B. T. Tang, S. Bruschi, A. Ghiotti, P. F. Bariani, *Finite Elem. Anal. Des.* **2014**, *81*, 69.
- [28] R. George, A. Bardelcik, M. J. Worswick, *J. Mater. Process. Technol.* **2012**, *212*, 2386.

- [29] J. Min, J. Lin, Y. Min, *J. Mater. Process. Technol.* **2013**, 213, 818.
- [30] T. K. Eller, L. Greve, M. Andres, M. Medricky, V. T. Meinders, A. H. Van Den Boogaard, *J. Mater. Process. Technol.* **2016**, 228, 43.
- [31] T. K. Eller, L. Greve, M. T. Andres, M. Medricky, A. Hatscher, V. T. Meinders, A. H. Van Den Boogaard, *J. Mater. Process. Technol.* **2014**, 214, 1211.
- [32] C. C. Tasan, J. P. M. Hoefnagels, M. Diehl, D. Yan, F. Roters, D. Raabe, *Int. J. Plast.* **2014**, 63, 198.
- [33] M. Diehl, D. Wang, C. Liu, J. Rezaei Mianroodi, F. Han, D. Ma, P. J. J. Kok, F. Roters, P. Shanthraj, *Adv. Eng. Mater.* **2020**, 22, 1901044.
- [34] L. Morsdorf, O. Jeannin, D. Barbier, M. Mitsuhashi, D. Raabe, C. C. Tasan, *Acta Mater.* **2016**, 121, 202.
- [35] J. Cui, Y. S. Chu, O. O. Famodu, Y. Furuya, J. Hatrick-Simpers, R. D. James, A. Ludwig, S. Thienhaus, M. Wuttig, Z. Zhang, I. Takeuchi, *Nat. Mater.* **2006**, 5, 286.
- [36] D. Yan, C. C. Tasan, D. Raabe, *Acta Mater.* **2015**, 96, 399.
- [37] C. A. Sciammarella, H. Nyuko, *Exp. Mech.* **1974**, 14, 311.
- [38] C. A. Sciammarella, D. L. Sturgeon, *Exp. Mech.* **1967**, 7, 468.
- [39] C. A. Sciammarella, *ASME* **1971**.
- [40] Y. Y. Hung, I. M. Daniel, R. E. Rowlands, *Exp. Mech.* **1978**, 18, 56.
- [41] T. D. Dudderar, P. G. Simpkins, *Nature* **1977**, 270, 45.
- [42] J. M. Carlson, J. E. Bird, *Acta Metall.* **1987**, 35, 1675.
- [43] A. Eisenlohr, I. Gutierrez-Urrutia, D. Raabe, *Acta Mater.* **2012**, 60, 3994.
- [44] Z. Zhao, M. Ramesh, D. Raabe, A. M. Cuitiño, R. Radovitzky, *Int. J. Plast.* **2008**, 24, 2278.
- [45] D. Raabe, M. Sachtleber, H. Weiland, G. Scheele, Z. Zhao, *Acta Mater.* **2003**, 51, 1539.
- [46] D. Raabe, M. Sachtleber, Z. Zhao, F. Roters, S. Zaeferrer, *Acta Mater.* **2001**, 49, 3433.
- [47] A. Martínez, R. Rodríguez-Vera, J. A. Rayas, H. J. Puga, *Opt. Lasers Eng.* **2003**, 39, 525.
- [48] D. P. Nicoletta, A. E. Nicholls, J. Lankford, D. T. Davy, *J. Biomech.* **2001**, 34, 135.
- [49] S. W. Khoo, S. Karuppanan, C. S. Tan, *Metrol. Meas. Syst.* **2016**, 23, 461.
- [50] M. Palanca, G. Tozzi, L. Cristofolini, *Int. Biomech.* **2016**, 3, 1.
- [51] A. Freddi, G. Olmi, L. Cristofolini, *Experimental Stress Analysis for Materials and Structures: Stress Analysis Models for Developing Design Methodologies*, Springer, Berlin/New York **2015**.
- [52] S. V. Sajadifar, E. Scharifi, U. Weidig, K. Steinhoff, T. Niendorf, *Metals* **2020**, 10, 884.
- [53] J. Li Ning, Y. Tong Zhang, L. Huang, Y. Li Feng, *Mater. Des.* **2017**, 120, 280.
- [54] R. Blenkinsopp, J. Roberts, A. Harland, P. Sherratt, P. Smith, T. Lucas, *Appl. Sci.* **2019**, 9, 2828.
- [55] F. Grytten, H. Daiyan, M. Polanco-Loria, S. Dumoulin, *Polym. Test.* **2009**, 28, 653.
- [56] L. Morin, J. B. Leblond, A. A. Benzerga, *J. Mech. Phys. Solids* **2015**, 75, 140.
- [57] A. Pineau, A. A. Benzerga, T. Pardoen, *Acta Mater.* **2016**, 107, 424.
- [58] C. C. Tasan, M. Diehl, D. Yan, C. Zambaldi, P. Shanthraj, F. Roters, D. Raabe, *Acta Mater.* **2014**, 81, 386.
- [59] R. bin Gou, W. jiao Dan, W. gang Zhang, M. Yu, C. yu Zhang, Y. hu Qiao, L. Ma, *J. Iron Steel Res. Int.* **2017**, 24, 350.
- [60] T. J. Rupert, *J. Appl. Phys.* **2013**, 114, 033527.
- [61] A. A. Benzerga, N. Thomas, J. S. Herrington, *Sci. Rep.* **2019**, 9, 1.
- [62] K. Ushioda, W. B. Hutchinson, *ISIJ Int.* **1989**, 29, 862.
- [63] K. Renard, S. Ryelandt, P. J. Jacques, *Mater. Sci. Eng., A* **2010**, 527, 2969.
- [64] R. Zhang, P. Bai, D. Lei, R. Xiao, *Int. J. Solids Struct.* **2018**, 146, 203.
- [65] R. Hill, *J. Mech. Phys. Solids* **1952**, 1, 19.
- [66] H. Ait-Amokhtar, P. Vacher, S. Boudrahem, *Acta Mater.* **2006**, 54, 4365.
- [67] R. C. Batra, B. M. Love, *J. Therm. Stress.* **2005**, 28, 747.
- [68] N. Jia, F. Roters, P. Eisenlohr, C. Kords, D. Raabe, *Acta Mater.* **2012**, 60, 1099.
- [69] N. Jia, D. Raabe, X. Zhao, *Acta Mater.* **2016**, 111, 116.
- [70] D. Dorner, S. Zaeferrer, D. Raabe, *Acta Mater.* **2007**, 55, 2519.
- [71] N. Jia, P. Eisenlohr, F. Roters, D. Raabe, X. Zhao, *Acta Mater.* **2012**, 60, 3415.
- [72] Q. Wu, M. A. Zikry, *Int. J. Solids Struct.* **2014**, 51, 4345.
- [73] J. F. C. Lins, H. R. Z. Sandim, H. J. Kestenbach, D. Raabe, K. S. Vecchio, *Mater. Sci. Eng., A* **2007**, 457, 205.
- [74] C. C. Tasan, M. Diehl, D. Yan, M. Bechtold, F. Roters, L. Schemmann, C. Zheng, K. Tsuzaki, N. Peranio, D. Ponge, M. Koyama, K. Tsuzaki, D. Raabe, *Annu. Rev. Mater. Res.* **2015**, 45, 391.
- [75] E. Hornbogen, G. Eggeler, E. Werner, *Aufbau Und Eigenschaften von Keramik-, Metall-, Polymer- Und Verbundwerkstoffen*, Springer-Verlag, Berlin Heidelberg **2012**.
- [76] D. Shi, P. Hu, L. Ying, *Int. J. Adv. Manuf. Technol.* **2016**, 84, 895.
- [77] J. Tong, *Fatigue Fract. Eng. Mater. Struct.* **2018**, 41, 1855.
- [78] M. Calcagnotto, Y. Adachi, D. Ponge, D. Raabe, *Acta Mater.* **2011**, 59, 658.
- [79] E. Scharifi, S. V. Sajadifar, G. Moeini, U. Weidig, S. Böhm, T. Niendorf, K. Steinhoff, *Adv. Eng. Mater.* **2020**, 2000193.